



**HAL**  
open science

# Sunlight activated ultra-stable long persistent luminescence glass ceramic for outdoor information display

Jingtao Zhao, Lei Lei, Renguang Ye, Junjie Zhang, Xianghua Zhang, Shiqing Xu

## ► To cite this version:

Jingtao Zhao, Lei Lei, Renguang Ye, Junjie Zhang, Xianghua Zhang, et al.. Sunlight activated ultra-stable long persistent luminescence glass ceramic for outdoor information display. *Journal of Advanced Ceramics*, 2022, 11 (6), pp.974-983. 10.1007/s40145-022-0595-1 . hal-03688061

**HAL Id: hal-03688061**

**<https://hal.science/hal-03688061>**

Submitted on 3 Jun 2022

**HAL** is a multi-disciplinary open access archive for the deposit and dissemination of scientific research documents, whether they are published or not. The documents may come from teaching and research institutions in France or abroad, or from public or private research centers.

L'archive ouverte pluridisciplinaire **HAL**, est destinée au dépôt et à la diffusion de documents scientifiques de niveau recherche, publiés ou non, émanant des établissements d'enseignement et de recherche français ou étrangers, des laboratoires publics ou privés.



Distributed under a Creative Commons Attribution 4.0 International License

# Sunlight activated ultra-stable long persistent luminescence glass ceramic for outdoor information display

Jingtao ZHAO<sup>a,b</sup>, Lei LEI<sup>a,\*</sup>, Renguang YE<sup>a</sup>, Junjie ZHANG<sup>a</sup>,  
Xianghua ZHANG<sup>b</sup>, Shiqing XU<sup>a,\*</sup>

<sup>a</sup>Key Laboratory of Rare Earth Optoelectronic Materials and Devices of Zhejiang Province, Institute of Optoelectronic Materials and Devices, China Jiliang University, Hangzhou 310018, China

<sup>b</sup>Laboratory of Glasses and Ceramics, Univ Rennes, CNRS, ISCR (Institute des Sciences Chimiques de Rennes) UMR CNRS 6226, University of Rennes 1, Rennes 35042, France

Received: January 30, 2022; Revised: March 26, 2022; Accepted: April 3, 2022

© The Author(s) 2022.

**Abstract:** Natural sunlight activated persistent luminescence (PeL) is ideal candidate for optical information display in outdoors without the requirement of electric supply. Except the brightness and duration, the stability especially water resistance of the PeL materials is of significant importance for practical application, which remains a great obstacle up to date. Herein, we report a new sunlight activated PeL glass ceramic containing hexagonal  $\text{Sr}_{13}\text{Al}_{22}\text{Si}_{10}\text{O}_{66}:\text{Eu}^{2+}$  crystals, which exhibits strong blue PeL and can last more than 200 h. The PeL can be charged by the full wavelengths located in AM 1.5G due to the broad distribution of traps in the crystal structure. The PeL is clearly observed by the naked eye even after 24 h upon sunlight irradiation irrespective of the weather, and the photoluminescence intensity only decreased ~3.3% after storing in water for 365 d. We demonstrate its potential application for thermal and stress responsive display as well as long-term continuous security indication upon sunlight irradiation, which not only save vast energy and reduce environment pollution, but also are appropriate for outdoor usage.

**Keywords:** solar energy; persistent luminescence (PeL); glass ceramic; optical information display; stability

## 1 Introduction

Optical information display attracts great attentions in many scenes, such as safety indication, emergency signs, traffic signage, and high temperature warnings. Photoluminescence, electroluminescence, and photo-responsive persistent luminescence (PeL) inorganic

materials, which exhibit adjustable emission wavelengths and strong brightness, are broadly used for display [1–5]. However, these materials require an electric supply to produce light, which not only waste a large amount of energy and bring environmental pollution, but also greatly limit their practical applications, especially in outdoors without power facilities [6,7].

Solar energy is environmentally friendly and inexhaustible, and the photon energies covering from ultra-violet (UV) to near infrared (NIR) are largely distributed near the ground. A few visible PeL phosphors can be activated by sunlight and last for a long time,

\* Corresponding authors.

E-mail: L. Lei, [leilei@cjlu.edu.cn](mailto:leilei@cjlu.edu.cn);

S. Xu, [shiqingxu@cjlu.edu.cn](mailto:shiqingxu@cjlu.edu.cn)

such as  $\text{Ba}_5\text{Si}_8\text{O}_{21}:\text{Eu}^{2+}/\text{Dy}^{3+}$  (473 nm, > 16 h),  $\text{SrAl}_2\text{O}_4:\text{Eu}^{2+}/\text{Dy}^{3+}$  (520 nm, > 10 h),  $\text{BaSiO}_3:\text{Eu}^{2+}/\text{Nd}^{3+}/\text{Tm}^{3+}$  (560 nm, > 10 h),  $\text{Sr}_3\text{SiO}_5:\text{Eu}^{2+}/\text{Nb}^{5+}$  (580 nm, > 14 h), and  $\text{Sr}_3\text{Y}_2\text{Ge}_3\text{O}_{12}:\text{Bi}^{3+}$  (354, 465, and 730 nm, > 60 h), which show promising application in optical information display [8–11]. For practical display in outdoors, except the brightness and duration, the stability especially water resistance is a very important performance index as well. However, most phosphors are moisture susceptible. Although coating organics on the surface of phosphors were used to isolate water molecules, the synthetic procedures are complex and the organics are prone to aging [12]. Another effective strategy for the improvement of phosphor stability is fabricating phosphor-in-glass structure, but the stringent glass components and multiple preparation steps are required [13,14]. Glass ceramic possesses excellent optical properties of crystals and superior stability of glass as well as simplified synthetic procedure, which has not been employed to generate sunlight activated PeL yet.

In this work, a new sunlight activated PeL glass ceramic containing hexagonal  $\text{Sr}_{13}\text{Al}_{22}\text{Si}_{10}\text{O}_{66}$  crystals (named as GC) was successfully developed for the first time.  $\text{Si}_3\text{N}_4$  was used to modify the glass structure for the precipitation of pure crystals without impurity phases. After incorporating  $\text{Eu}^{2+}$  into the crystal structure (named as GC:Eu), it exhibited full wavelengths in AM 1.5G responsive ultra-long PeL owing to the broad trap distributions. Its PeL lasted more than 200 h upon excitation by a 365 nm lamp for 5 min and over 24 h after sunlight irradiation for 15 min irrespective of the weather. Moreover, the GC:Eu possessed much superior stability even after it was preserved in water for 365 d. We successfully demonstrated the promising application of the studied GC:Eu for stress and temperature responsive display as well as long-term continuous security indication.

## 2 Experimental

### 2.1 Materials and preparation

The glasses with the compositions of  $49.7\text{SrO}-12.5\text{Al}_2\text{O}_3-31.4\text{SiO}_2-x\text{Eu}_2\text{O}_3-y\text{Si}_3\text{N}_4$  ( $x = 0.05, 0.1, 0.3, 0.5, \text{ and } 1; y = 0 \text{ and } 6.3$ ) were prepared by the typical melt-quenching method. High-purity  $\text{SiO}_2$  (99.99%),  $\text{Al}_2\text{O}_3$  (99.99%),  $\text{Sr}_2\text{CO}_3$  (99.99%),  $\text{Si}_3\text{N}_4$  (99.99%), and  $\text{Eu}_2\text{O}_3$  (99.99%) purchased from

Aladdin Chemical Reagent Company without any further treatment were used as raw materials. In a detailed synthetic procedure, 20 g raw materials with the designed stoichiometric ratio were mixed and ground thoroughly in an agate mortar manually for 30 min. Then the mixture was transferred into a covered alumina crucible and melted at 1580 °C for 4 h in CO reducing atmosphere to achieve  $\text{Eu}^{2+}$ . The melt was quenched on a stainless steel plate at 500 °C to form bulk glass. The precursor glass was obtained by annealing at 750 °C for 3 h, and the glass ceramic was achieved by heat treatment at higher temperature (975, 1000, 1025, or 1050 °C) for 5 h. All the glass and glass ceramic samples were cut and polished to a thickness of 2 mm for structure and performance characterizations.

### 2.2 Characterization

The thermal properties of the glass sample were measured by a differential thermal analysis (DTA) method using a Netzsch DTA 404PC at a heating rate of 10 K/min. The crystallization properties of the glass and GCs were identified by X-ray diffraction (XRD) using a Bruker D2 PHASER ( $\text{Cu K}\alpha_1, \lambda = 0.15406 \text{ nm}$ , 30 kV, 10 mA) in the range of  $10^\circ-80^\circ$  with a step size of  $0.1^\circ$ . Rietveld XRD refinement was conducted using TOPAS 4.2 software. Transmission electron microscopy (TEM) and high-resolution TEM (HRTEM) images of the glass ceramics were carried out by a transmission electron microscope (FEI Tecnai G2 F20). Scanning electron microscopy (SEM) image and element mapping were performed by a field emission scanning electron microscope (Hitachi SU8010) with an energy dispersive X-ray spectroscopy (EDS) system. Raman spectra of the glass and glass ceramics were measured by a Renishaw inVia Raman microscope using 532 nm line as the excitation source. Fourier-transform infrared (FTIR) spectra were performed by a Bruker vector 33 spectrometer. X-ray photoelectron spectroscopy (XPS) was conducted by a Thermo Scientific K-Alpha photoelectron spectrometer. Diffuse reflectance spectrum was recorded by a Shimadzu UV-3600 spectrometer in the range of 200–800 nm. Photoluminescence (PL) spectra, photoluminescence excitation (PLE) spectra, and PeL decay curves were performed by a fluorescence spectrophotometer (Jobin-Yvon Fluorolog3) equipped with a 450 W xenon lamp. The fluorescence decay was measured on the same spectrophotometer and a 365 nm Nano LED was employed as excitation source.

Thermoluminescence (TL) spectra of the glass ceramic was measured by a TOSL-3DS thermoluminescence spectrometer at a heating rate of 5 K/s after irradiating at 365 nm light for 10 min. X-ray excited luminescence (XEL) spectra was measured by grating spectrometer (Omni- $\lambda$ 300i, Zolix, China). The PeL photos were taken by a digital camera (Nikon D5500, auto mode). Before measuring PeL properties, the samples were heat treated at 500 °C for 30 min to empty the trap energies to prevent signal interferences. The PeL performance was performed in Hangzhou, Zhejiang, China (30°19'22" N and 120°22'21" E).

### 3 Results and discussion

#### 3.1 Microstructure analysis of the GC

DTA analysis (Fig. 1(a)) revealed that the glass transition temperature ( $T_g$ ), onset crystallization temperature ( $T_x$ ), and crystallization peak temperature ( $T_p$ ) of the product

were about 797, 975, and 1042 °C, respectively. The large  $\Delta T$  of 178 °C, which is a thermal stability factor and defined by  $T_x - T_g$ , suggested its superior thermal property [15]. As exhibited in Fig. S1 in the Electronic Supplementary Material (ESM), the as-prepared product exhibited an amorphous structure before heat treatment, while a crystal phase was precipitated in the glass matrix after heat treatment. The evidently intensified XRD peak intensity indicated that the crystallinity was significantly improved when the heat treatment temperature was increased. The glass ceramic heat treated at 1050 °C was used to study its microstructure and optical properties in this work. Although the standard JCPDS card was not found, the XRD pattern of hexagonal  $Ba_{13}Al_{22}Si_{10}O_{66}$  phase (ICSD#2940) could be employed as an ideal reference [16,17]. As shown in Fig. 1(b), all the diffraction peaks of the GC are almost identical to that of hexagonal  $Ba_{13}Al_{22}Si_{10}O_{66}$  except a slight shift toward higher angle owing to the smaller ionic radius of  $Sr^{2+}$  (0.121 nm, coordination number

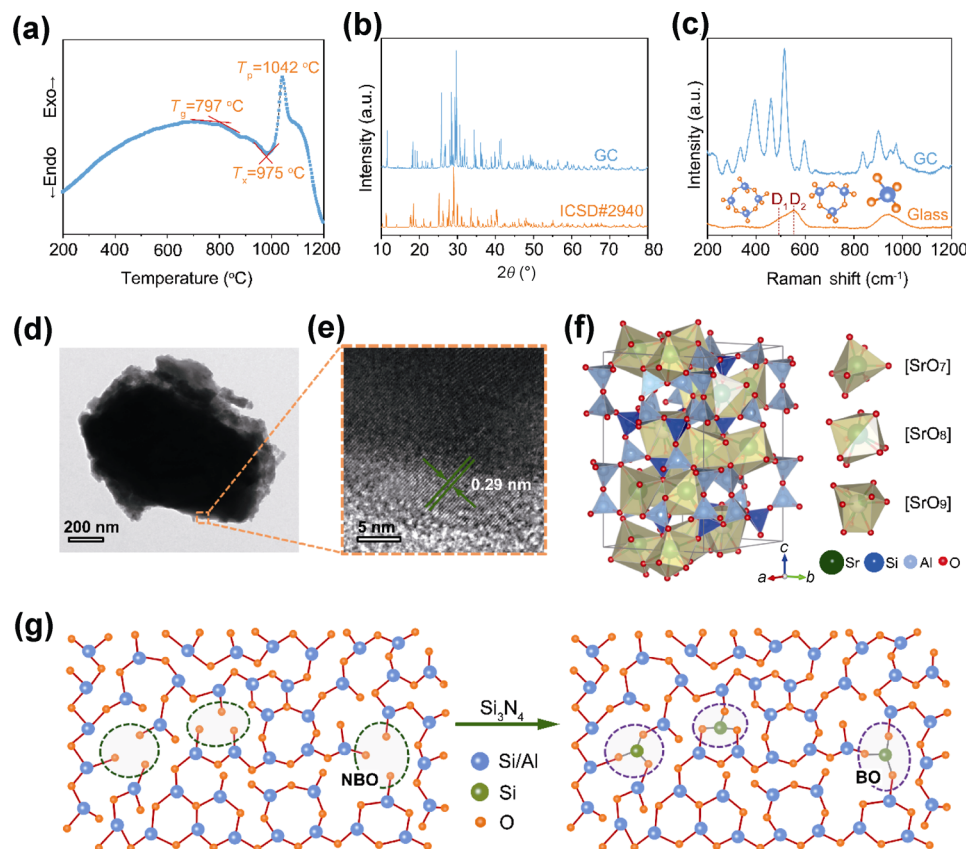


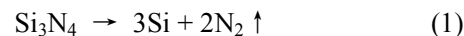
**Fig. 1** (a) DTA curve of the glass. (b) XRD patterns of the GC and standard hexagonal  $Ba_{13}Al_{22}Si_{10}O_{66}$  phase (ICSD#2940). (c) Raman spectra of the glass and GC. Inset is the stretching unit structures corresponding to different Raman peaks. Low magnification TEM (d) and HRTEM (e) images of the GC. (f) Crystal structure of the  $Sr_{13}Al_{22}Si_{10}O_{66}$  and  $[SrO_x]$  units. (g) Schematic illustration of the two-dimensional structure of the glass with (left) and without (right)  $Si_3N_4$ . The oxygens in the green and purple circles represent the non-bridging oxygens (NBO) and bridging oxygens (BO), respectively.

CN = 7) than that of  $\text{Ba}^{2+}$  (0.138 nm, CN = 7) ions. Therefore, we confirm that the precipitated crystal is belonged to hexagonal  $\text{Sr}_{13}\text{Al}_{22}\text{Si}_{10}\text{O}_{66}$  phase. According to the refinement result shown in Fig. S2 in the ESM, the GC was in accordance well with the hexagonal crystal structure. The lattice parameters were calculated to be  $a = b = 7.95 \text{ \AA}$  and  $c = 16.59 \text{ \AA}$ , and Sr atoms were located at three different positions of (0.6881, 0.0944, 0.0000), (0.8835, 0.2547, 0.2913), and (0.3333, 0.6667, 0.0941). TEM and HRTEM images (Figs. 1(d) and 1(e), respectively) manifest the high crystallinity and single crystal nature of the analyzed particle.

Raman (Fig. 1(c)) and FTIR (Fig. S3 in the ESM) spectra were used to reveal the structural evolution from glass to GC. Raman spectrum of the as-prepared glass was well in accordance with the characteristic peaks of aluminosilicate glass. Specifically, the strong band at  $560 \text{ cm}^{-1}$  ( $\text{D}_2$ ) and a shoulder at  $498 \text{ cm}^{-1}$  ( $\text{D}_1$ ) are corresponding to the O breathing symmetric stretching in four- and three-membered rings of  $\text{TO}_4$  ( $\text{T} = \text{Al}$  or  $\text{Si}$ ) tetrahedra, respectively, while that of located in the range of  $850\text{--}1050 \text{ cm}^{-1}$  is assigned to the Si–O stretching in  $\text{SiO}_4$  tetrahedra [18–20]. After the precipitation of  $\text{Sr}_{13}\text{Al}_{22}\text{Si}_{10}\text{O}_{66}$  crystals, these characteristic peaks were split into several sharp ones. The appearance of peaks at 279, 334, and  $394 \text{ cm}^{-1}$  is attributed to the vibration of  $\text{Sr}^{2+}$  and the coupled vibration of Sr–O and  $\text{TO}_4$  in a long-range order crystal structure [21,22]. The peaks at 460, 515, and  $595 \text{ cm}^{-1}$  are ascribed to the bending vibrations of bridging oxygen bonds in Si–O and motions of bridge oxygen in T–O–T linkages, and that of 837, 900, and  $974 \text{ cm}^{-1}$  are assigned to the symmetric vibrations of non-bridging and bridging oxygens [21,22]. Similarly, as revealed by the FTIR spectra, the broad absorption bands located in  $400\text{--}550$ ,  $600\text{--}800$ , and  $800\text{--}1200 \text{ cm}^{-1}$ , which were corresponding to the bending vibrations of Si–O–Si (Si–O–Al) linkages, stretching vibrations of the Al–O bonds in  $[\text{AlO}_4]$  tetrahedron and the stretching vibrations of the  $[\text{SiO}_4]$  tetrahedron, respectively, were split after the formation of  $\text{Sr}_{13}\text{Al}_{22}\text{Si}_{10}\text{O}_{66}$  crystal as well [23]. As illustrated in Fig. 1(f), the crystal structure of  $\text{Sr}_{13}\text{Al}_{22}\text{Si}_{10}\text{O}_{66}$  is composed of  $[\text{TO}_4]$  tetrahedrons and  $[\text{SrO}_x]$  units containing  $[\text{SrO}_7]$ ,  $[\text{SrO}_8]$ , and  $[\text{SrO}_9]$ . When activators with 5d–4f transitions are occupied in the  $\text{Sr}^{2+}$  lattice with multiple coordinates, many intriguing optical phenomena might be discovered.

It is worth to mention that the  $\text{Si}_3\text{N}_4$  is requisite for the formation of pure hexagonal  $\text{Sr}_{13}\text{Al}_{22}\text{Si}_{10}\text{O}_{66}$  phase.

As shown in Fig. S4 in the ESM, without the addition of  $\text{Si}_3\text{N}_4$ , two mixture crystal phases of  $\text{SrAl}_2\text{Si}_2\text{O}_8$  and  $\text{Sr}_2\text{Al}_2\text{SiO}_7$  were emerged in the XRD pattern. Raman spectra of the glass products (Fig. S5 in the ESM) revealed that the Si–O stretching vibration peak shifted toward high frequency by  $20 \text{ cm}^{-1}$  after the addition of  $\text{Si}_3\text{N}_4$ , indicating that the  $\text{Si}_3\text{N}_4$  promoted the reduction of non-bridging oxygens which were generally formed in the amorphous glass structure [24]. During the glass melting process at high temperature, the  $\text{Si}_3\text{N}_4$  could be decomposed via the following process [25]:



In such case,  $\text{N}_2$  is volatilized from the glass system, while the Si atoms are preserved in the glass system which benefits the transformation of non-bridging oxygen to bridging ones (Fig. 1(g)).

### 3.2 Photoluminescence properties of the non-doped GC

Under 277 nm light excitation, the glass exhibited broad emission from 300 to 700 nm with peaking at 460 nm, whose intensity was enhanced about 3.6 times after heat treatment owing to the increased crystallinity (Fig. 2(a)). This broad emission is ascribed to the existence of defects in the crystal structure because there is no activator in the glass and GC [26]. During the melt process with CO-rich reducing atmosphere, many oxygen vacancies are favorable to be formed in the glass system and preserved in the GC via in-situ precipitation [27], which lead to the generation of traps in the glass and crystal structures. The photoluminescence (PL) profile in the range of  $14,285.74\text{--}33,333.33 \text{ cm}^{-1}$  of the GC is asymmetric, which can be fitted into three emissions peaking at  $\sim 26,429.02 \text{ cm}^{-1}$  (trap 1),  $\sim 22,123.89 \text{ cm}^{-1}$  (trap 2), and  $\sim 19,685.04 \text{ cm}^{-1}$  (trap 3) (Fig. 2(d)). Similarly, the PL spectra of the glass were fitted into two emission peaking at  $\sim 23,414.36 \text{ cm}^{-1}$  (trap 2) and  $\sim 20,618.56 \text{ cm}^{-1}$  (trap 3) (Fig. 2(c)). By comparison the PL spectra between the glass and GC, it is reasonable to deduce that trap 2 and trap 3 are produced in the glass melt-quenching process and preserved in the GC, while trap 1 is generated during the heat treatment process. As shown in Fig. S6 in the ESM, the TL spectra of GC were fitted into three peaks (326, 364, and 397 K), suggesting the existence of three kinds of traps. According to the Kubelka–Munk function [28], the band gap of the GC is calculated to be about 4.61 eV based on the measured diffuse reflectance

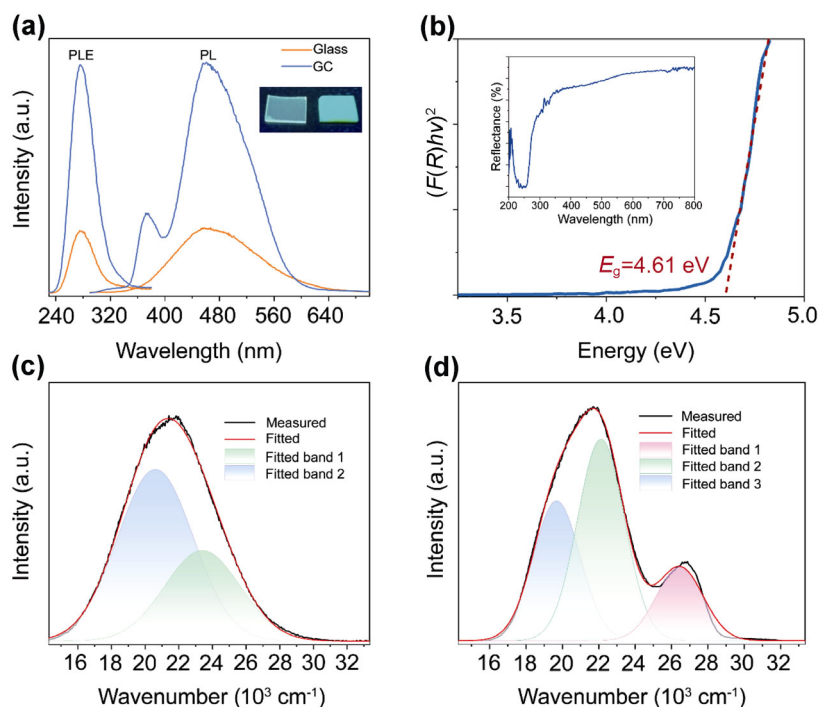


**Fig. 2** (a) PL and PLE spectra of non-doped glass and GC. Inset is photographs of the glass (left) and GC (right) under 254 nm light excitation. (b) Converted diffuse reflectance spectrum of the  $\text{Sr}_{13}\text{Al}_{22}\text{Si}_{10}\text{O}_{66}$  host via a Kubelka–Munk function. The bandgap energy was estimated from the intercept of a fitted red dotted line. Inset is the diffuse reflectance spectrum of the GC. Fitted PL spectra of the glass (c) and GC (d).

spectrum (Fig. 2(b)), which is consistent with the photoluminescence excitation (PLE) at 277 nm (4.48 eV). The profiles of the PLE spectra monitored at 460 and 373 nm in the GC as well as 460 nm in the glass were similar, indicating that all of these radiative transition states were populated by the absorbed input photons via band gap transitions (Figs. 2(a) and S7 in the ESM).

The broad PL spectra of the GC indicate the wide distribution of traps in the  $\text{Sr}_{13}\text{Al}_{22}\text{Si}_{10}\text{O}_{66}$  crystal structure, which benefits the generation of PeL emission. However, the initial PeL intensity of the present studied GC is only  $\sim 0.74\%$  of its PL intensity, which is too weak to be observed by the naked eye (Fig. S8 in the ESM). This poor PeL performance is mainly attributed to the absence of suitable activators, which inspires us to study the divalent  $\text{Eu}^{2+}$  ion incorporated GC (named as GC:Eu).

### 3.3 Luminescence properties of the $\text{Eu}^{2+}$ -doped GC

XRD patterns (Fig. S9 in the ESM) verified that pure GC:Eu with different Eu concentrations were achieved. The XRD peaks shift toward higher angles with an increase of Eu doping concentration, which is due to the incorporation of  $\text{Eu}^{2+}$  with smaller ionic radius

(0.12 nm, CN = 7) via substituting  $\text{Sr}^{2+}$  in the  $\text{Sr}_{13}\text{Al}_{22}\text{Si}_{10}\text{O}_{66}$  crystal structure. EDS mapping results further revealed the existence of Eu elements (Fig. S10 in the ESM). As shown in Fig. 3(a), the broad PL emissions in 385–625 nm corresponding to  $\text{Eu}^{2+}$ :  $4f^65d^1 \rightarrow 4f^7$  were recorded under 365 nm light excitation. With monitoring the emission at 450 nm, the broad PLE spectra from 200 to 420 nm were observed for all the studied  $\text{Eu}^{2+}$  doped GCs. The optimal Eu doping concentration was measured to be about 0.2 mol%, whose lifetime was about 241 ns (Fig. S11 in the ESM). Interestingly, the PL spectra can be fitted into three emission bands peaking at 23,364.49, 22,172.95, and 20,790.02  $\text{cm}^{-1}$  (Fig. S12 in the ESM), manifests that the  $\text{Eu}^{2+}$  ions are distributed in three  $[\text{SrO}_8]$ ,  $[\text{SrO}_7]$ , and  $[\text{SrO}_9]$  units with different coordinates [29]. XPS analysis confirmed that the divalent  $\text{Eu}^{2+}$  and trivalent  $\text{Eu}^{3+}$  were co-existed in the GC:Eu (Fig. S13 in the ESM), and the calculated doping contents of  $\text{Eu}^{2+}$  and  $\text{Eu}^{3+}$  were about 0.064 and 0.136 mol%, respectively [30]. Due to the spin-forbidden  $\text{Eu}^{3+}$ :  $4f-4f$  transition and its low doping concentration, the PL intensity of  $\text{Eu}^{3+}$  was much weaker than that of parity allowed  $\text{Eu}^{2+}$ :  $5d-4f$  transition [31].

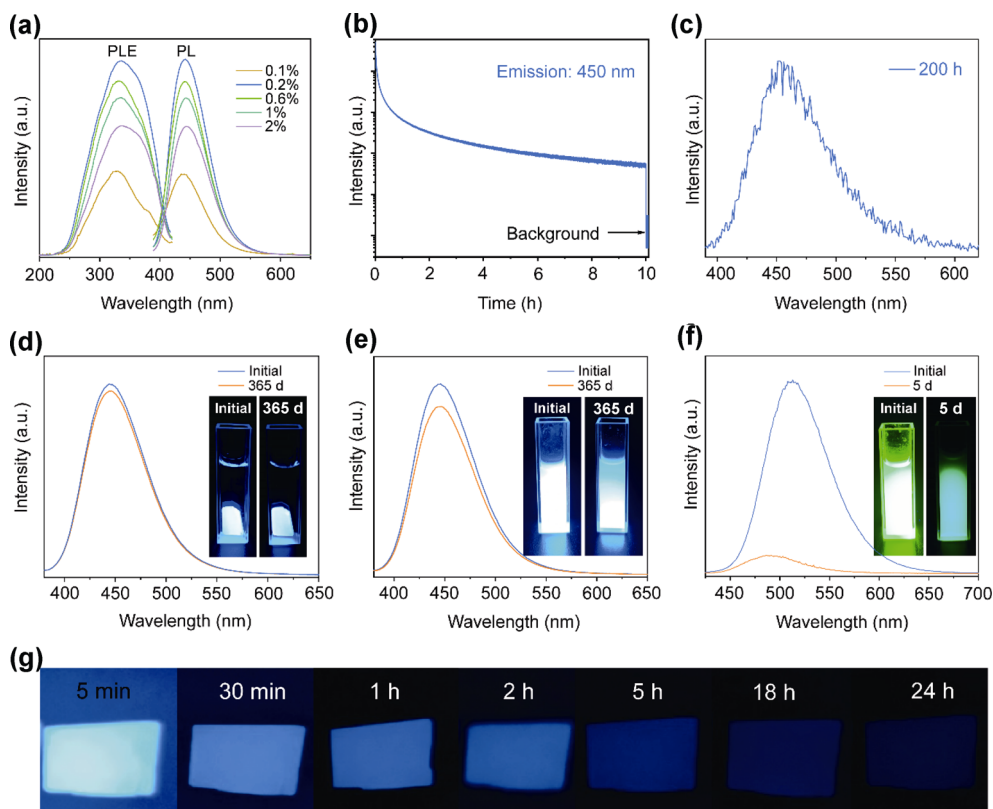


**Fig. 3** (a) PL and PLE spectra of the  $\text{Eu}^{2+}$  doped GC with different concentrations. (b) PeL decay curve of the 0.2 mol%  $\text{Eu}$  doped GC:Eu monitored at 450 nm. The sample was irradiated by 365 nm light for 5 min. (c) PeL spectra after 200 h. (d, e, f) PL spectra of the bulk GC:Eu, GC:Eu powder, and commercial  $\text{AlSr}_2\text{O}_4:\text{Eu}^{2+}/\text{Dy}^{3+}$  phosphor before and after storing in water, respectively. Insets are their corresponding photographs under 365 nm light excitation. (g) PeL photographs of the GC:Eu recorded at different time after cessation of 365 nm light.

Interestingly, different from the GC, the GC:Eu show bright and ultra-long PeL. The optimal Eu doping concentration for PeL was also measured to be about 0.2 mol% (Figs. S14 and S15 in the ESM). After irradiation by a 365 nm lamp for 5 min, the PeL decay curve revealed that the PeL intensity was still much stronger than the background after 10 h (Fig. 3(b)), and the measured spectrum suggested that the PeL could last more than 200 h (Figs. 3(c) and S16 in the ESM). As shown in Fig. 3(g), the bright blue PeL can be clearly observed by the naked eye after 24 h. It has been reported that the  $\text{SrAl}_2\text{Si}_2\text{O}_8$  and  $\text{Sr}_2\text{Al}_2\text{SiO}_7$  matrixes are both suitable for the incorporation of  $\text{Eu}^{2+}$  ions followed by the strong and long PeL [32,33]. As shown in Fig. S17 in the ESM, the  $\text{Eu}^{2+}$  doped glass ceramic containing mixed  $\text{SrAl}_2\text{Si}_2\text{O}_8$  and  $\text{Sr}_2\text{Al}_2\text{SiO}_7$  phases showed much lower initial PeL intensity as well as faster decay rate than that of GC:Eu, which further manifested the superior PeL performances of the hexagonal  $\text{Sr}_{13}\text{Al}_{22}\text{Si}_{10}\text{O}_{66}:\text{Eu}^{2+}$  crystals.

Stability of the GC:Eu is further studied to show its

possibility for practical application. The GC:Eu was irradiated by 365 nm light for 3 min and then its PeL decay curve was recorded, which was repeated for 100 times to show its highly rechargeable performance. As shown in Fig. S18 in the ESM, the initial PeL intensity, as well as its decay curve were almost kept unchanged during the measured 100 cycles. Besides, as shown in Fig. 3(d), after storing the GC:Eu in water for 365 d under natural environment, its PL intensity only decreased about 3.4%, and the bright blue luminescence was clearly observed under 365 nm light excitation as well. More importantly, the PeL decay curves of the GC:Eu was almost kept unchanged after preserving in water for 365 d (Fig. S19 in the ESM). Furthermore, when the GC:Eu was grinded into powder and then dispersed in water for 365 d, its PL intensity only decreased about 11.7%, and the bright blue color was recorded (Fig. 3(e)). As shown in Fig. 3(f), the strong PL emission was recorded in the commercial  $\text{SrAl}_2\text{O}_4:\text{Eu}^{2+}/\text{Dy}^{3+}$  PeL phosphor; however, its PL intensity was significantly decreased about 90.7% with peaking shift

from 515 to 490 nm after storing in water for only 5 d. The emission color change from green to bluish green was clearly verified by our naked eye. These results manifested that the present studied GC:Eu possesses excellent stability, which is much superior to that of commercial SrAl<sub>2</sub>O<sub>4</sub>:Eu<sup>2+</sup>/Dy<sup>3+</sup> phosphor.

### 3.4 Mechanistic study of the PeL

Thermoluminescence (TL) was used to reveal the depth of defects formed in the GC:Eu. As shown in Fig. 4(a), the asymmetric TL spectrum in the range of 270–550 K, could be well fitted into three bands peaking at 333, 361, and 393 K, which indicated the existence of three types of traps inside the GC:Eu. This result is consistent with the PL (Fig. 2(d)) and TL (Fig. S6 in the ESM) spectra of the GC product. The depth of these three traps was calculated to be 0.666, 0.722, and 0.786 eV based on the Urbach formula [34]:

$$E = T_m/500 \tag{2}$$

where  $E$  (eV) is the depth of the trap and  $T_m$  (K) is the peak temperature. The broad TL band suggests the wide distribution of traps, which shortens the distances between traps and activators followed by the improved electrons capturing efficiency [35]. Moreover, as shown

in Fig. 4(b) and Fig. S20 in the ESM, the full wavelengths of sunlight located in AM 1.5G could be used to excite the GC:Eu, and thus, its PeL was efficiently activated by natural sunlight. As shown in Fig. S21 in the ESM, after exposed to sunlight for 15 min, the bright PeL was clearly observed, which lasted for more than 24 h. Interestingly, as exhibited in Fig. S22 in the ESM, this superior PeL performance can be realized in various weather conditions (i.e., sunny, cloudy, and rainy) at different time (8:00, 12:00, and 17:00). Furthermore, the white light LED covers the whole visible region (Fig. S23 in the ESM), which can be used to stimulate the GC:Eu to produce strong PeL as well (Fig. 4(c)). It should be noted that the weak PeL after 24 h could be brightened again through heating (Fig. S24 in the ESM), indicating that the deep traps with a slow electron releasing rate could capture many electrons as well.

Based on the above analysis, a possible mechanism for the above strong and ultra-long PeL is proposed (Fig. 4(d)). Upon UV irradiation, the photon energies are absorbed via Eu<sup>2+</sup>: 4f→5d transition (process 1). Part of these excited electrons are relaxed to the ground state followed by the generation of PL emission, while part of them are captured by traps through the conduction band which is near the Eu<sup>2+</sup>: 5d state

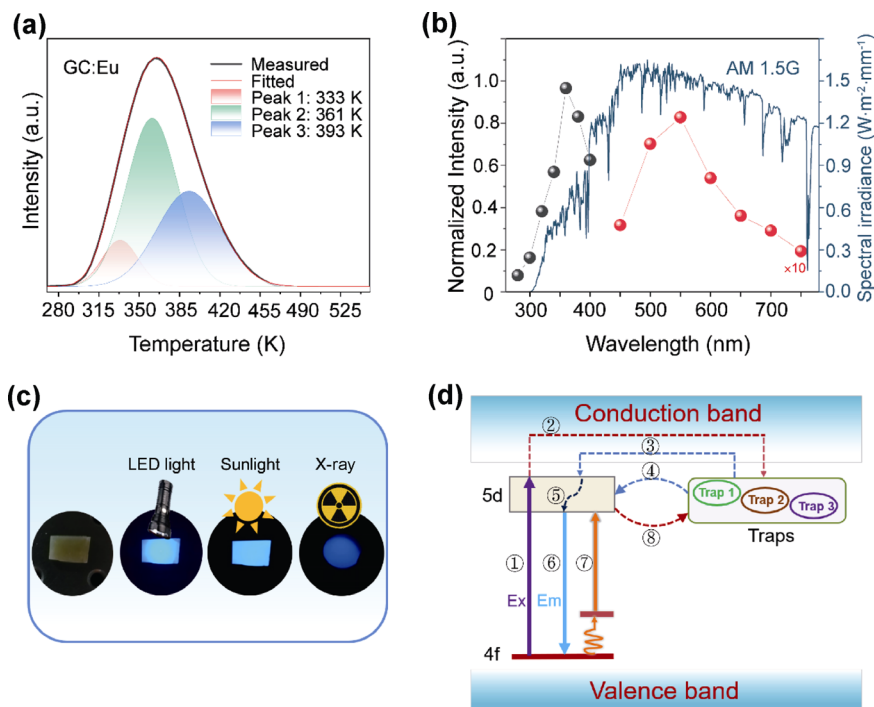


**Fig. 4** (a) TL spectra of the GC:Eu in the range of 270–550 K at a heating rate of 5 K/s. Before testing, the sample was irradiated by 365 nm light for 10 min. (b) PeL intensity of the GC:Eu versus irradiation wavelength in AM 1.5G. (c) PeL photographs of the GC:Eu excited by different light source (white LED, sunlight, and X-ray). (d) Schematic diagram of PeL luminescence mechanism.

(process 2). In the initial stage after the cessation of stimulation,  $\text{Eu}^{2+}$  5d state is populated again by the electrons released from the shallow traps (process 3), which contributes to the bright blue PeL emission (processes 5 and 6). The ultra-long PeL is mainly attributed to the existence of deep traps which could preserve a large number of electrons with a low releasing rate. These electrons are slowly transferred to the neighboring  $\text{Eu}^{2+}$  via tunneling process (processes 4–6) [36]. Under the visible light excitation, the  $\text{Eu}^{2+}$  can be excited to an intermediate state with the assistance of phonon energy (process 7) and then its 5d state was populated by the input photons [37,38]. In this case, the neighboring traps will be populated (process 8) followed by the PeL emission [37–39].

### 3.5 Information display application

The highly stable GC:Eu with strong and ultra-long PeL performance shows promising application for outdoor information display without the requirement of light source. The GC:Eu contained ink was prepared by dissolving its powder in water or ethanol (0.1 g/mL). When the ink was charged by sunlight for 15 min, the bright blue PeL was observed (Fig. 5(a)), and then became weak after about 3 h later (Fig. 5(b)). Interestingly, strong blue light was observed again through shaking the glass bottle for 1 min (Fig. 5(c)), and the PeL intensity was significantly intensified through magnetic stirring (Fig. S25 in the ESM), which was attributed to

the releasing of electrons from deep traps and could be employed for stress-related stimulus responsive display. In addition, the ink shown in Fig. 5(b) was used to write a letter “A” on a paper cup (Fig. 5(d)), which was invisible at room temperature. After pouring 50 °C water into the cup, the letter “A” was clearly appeared in 2 s, and the brightness was further increased by the addition of 100 °C water, which could be used for thermal responsive display. As shown in Fig. 5(g), when the numbers “123” wrote on an A4 paper was exposed to sunlight for 3 min, its bright PeL was lasted for more than 2 h. Moreover, a designed “EXIT” pattern was printed by the GC:Eu ink and then charged by sunlight for 20 min. Evidently, clear blue letters of “EXIT” were still observed by the naked eye even after 12 h (Fig. 5(h)). These results suggest that the present developed GC:Eu product is an ideal candidate for outdoor information display without the requirement of electric facilities.

Scintillators attract great attentions in the fields of security inspections, medical diagnosis and space exploration [40,41]. Especially, X-ray charged PeL is suitable for extension imaging and deep tissue bio-imaging [42–44]. As shown in Fig. S26 in the ESM, upon X-ray irradiation, the bulk GC:Eu sample exhibited stronger scintillation than that of commercial CsI:Tl crystal in the blue region, and the whole integrated intensity is ~56.4% of the CsI:Tl crystal. Moreover, the bright and long blue PeL was clearly observed after the cessation of X-rays (Figs. 4(c) and S27 in the ESM).

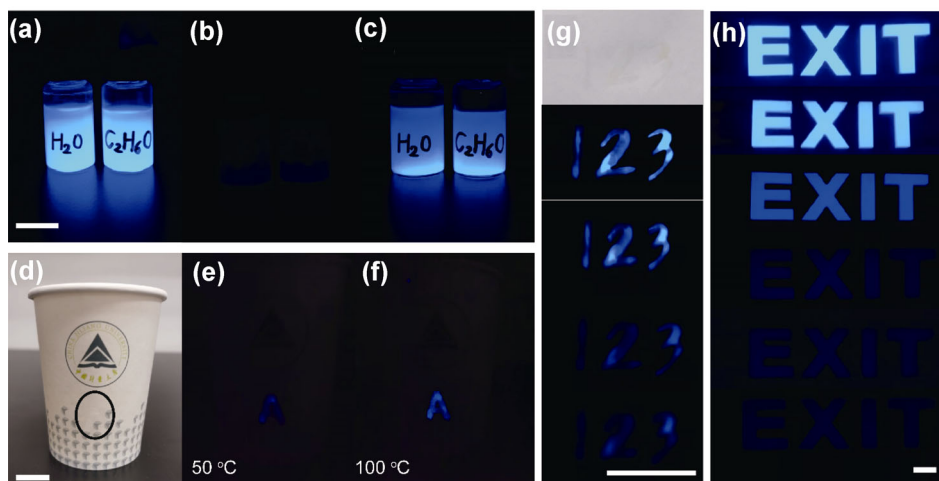


**Fig. 5** PeL photographs of the GC:Eu powder contained water and ethanol suspension at 1 min (a), 2 h (b) (sunlight irradiation for 15 min), and then shaking (role as an external force) the glass bottle for 1 min (c). (d) Paper cup with a letter “A” written in a black circle at room temperature. (e, f) PeL photographs with pouring 50 and 100 °C water into the cup. (g) Photographs of the handwritten numbers “123” on an A4 paper and the corresponding PeL at 5 min, 30 min, 1 h, and 2 h. (h) PeL photographs of the printed “EXIT” pattern at different time, from top to bottom are 10 min, 30 min, 1 h, 3 h, 6 h, and 12 h, respectively. The scale bar represents 15 mm.

Generally, heavy metal elements are employed to interact with X-ray photons to generate massive secondary electrons with low kinetic energy, but the atomic number of the heaviest Sr in our studied  $\text{Sr}_{13}\text{Al}_{22}\text{Si}_{10}\text{O}_{66}$  matrix is only 38. In this case, it is reasonable to estimate that the scintillation performance of the GC:Eu might be significantly improved by chemical composition tuning. Thus, investigation on  $\text{A}_{13}\text{B}_{22}\text{C}_{10}\text{O}_{66}$ -structure systems may promote the exploration of high performance scintillators for low-dose X-ray detection and imaging.

## 4 Conclusions

In conclusion, a new long PeL glass ceramic containing hexagonal  $\text{Sr}_{13}\text{Al}_{22}\text{Si}_{10}\text{O}_{66}:\text{Eu}^{2+}$  crystals was successfully developed.  $\text{Si}_3\text{N}_4$  precursor promoted the transformation of non-bridging oxygens to bridging ones, which guaranteed the precipitation of pure crystals. The PeL of GC:Eu can be activated by the full wavelengths located in AM 1.5G, which is attributed to the wide distribution of traps in the crystal structure. The PL and PeL of the GC:Eu showed excellent water stability owing to the glass structure. Its PeL lasted more than 200 h upon excitation by a 365 nm lamp for 5 min and over 24 h after natural sunlight irradiation for only 15 min. The sunlight activated long PeL characteristic makes it suitable for multimodal displays, such as thermal and stress responsive information display as well as long-term security instructions, without the demand of electric supply. The development of this new kind of sunlight chargeable ultra-long, stable, and bright PeL glass ceramic not only saves vast energy and reduces environmental pollution, but also extends its application scenarios.

## Acknowledgements

The authors thank National Natural Science Foundation of China (52172164, 51872270), National Key R&D Program of China (2018YFE0207700), Zhejiang Provincial Natural Science Foundation of China (LZ21A040002), and National Natural Science Foundation of China Joint Fund Project (U190920054).

## Declaration of competing interest

The authors have no competing interests to declare that are relevant to the content of this article.

## Electronic Supplementary Material

Supplementary material is available in the online version of this article at <https://doi.org/10.1007/s40145-022-0595-1>.

## References

- [1] Wang LD, Zhao ZF, Wei C, *et al.* Review on the electroluminescence study of lanthanide complexes. *Adv Opt Mater* 2019, **7**: 1801256.
- [2] Pulli T, Dönsberg T, Poikonen T, *et al.* Advantages of white LED lamps and new detector technology in photometry. *Light Sci Appl* 2015, **4**: e332.
- [3] Zhang H, Su Q, Chen S. Quantum-dot and organic hybrid tandem light-emitting diodes with multi-functionality of full-color-tunability and white-light-emission. *Nat Commun* 2020, **11**: 2826.
- [4] Li Y, Gecevicius M, Qiu JR. Long persistent phosphors—From fundamentals to applications. *Chem Soc Rev* 2016, **45**: 2090–2136.
- [5] MJain A, Kumar A, Dhoble SJ, *et al.* PL: An insight. *Renew Sust Energ Rev* 2016, **65**: 135–153.
- [6] Gu SQ, Guo HJ, Shi QF, *et al.* Sunlight-activated orange persistent luminescence from Bi-doped  $\text{SrBaZn}_2\text{Ga}_2\text{O}_7$  for warm-color optical applications. *Inorg Chem* 2021, **60**: 19233–19241.
- [7] Gong ZL, Zheng W, Gao Y, *et al.* Full-spectrum persistent luminescence tuning using all-inorganic perovskite quantum dots. *Angew Chem Int Ed* 2019, **58**: 6943–6947.
- [8] Jia YL, Sun WZ, Pang R, *et al.* Sunlight activated new long persistent luminescence phosphor  $\text{BaSiO}_3:\text{Eu}^{2+}, \text{Nd}^{3+}, \text{Tm}^{3+}$ : Optical properties and mechanism. *Mater Des* 2016, **90**: 218–224.
- [9] Zhou ZH, Wang X, Yi XD, *et al.* Rechargeable and sunlight-activated  $\text{Sr}_3\text{Y}_2\text{Ge}_3\text{O}_{12}:\text{Bi}^{3+}$  UV–visible–NIR persistent luminescence material for night-vision signage and optical information storage. *Chem Eng J* 2021, **421**: 127820.
- [10] Wang PJ, Xu XH, Zhou DC, *et al.* Sunlight activated long-lasting luminescence from  $\text{Ba}_5\text{Si}_8\text{O}_{21}:\text{Eu}^{2+}, \text{Dy}^{3+}$  phosphor. *Inorg Chem* 2015, **54**: 1690–1697.
- [11] Wang ZZ, Song Z, Ning LX, *et al.* Sunlight-activated yellow long persistent luminescence from Nb-doped  $\text{Sr}_3\text{SiO}_5:\text{Eu}^{2+}$  for warm-color mark applications. *J Mater Chem C* 2020, **8**: 1143–1150.
- [12] Bem DB, Luyt AS, Dejene FB, *et al.* Structural, luminescent and thermal properties of blue  $\text{SrAl}_2\text{O}_4:\text{Eu}^{2+}, \text{Dy}^{3+}$  phosphor filled low-density polyethylene composites. *Phys B Condens Matter* 2009, **404**: 4504–4508.
- [13] Zhang H, Zhao L, Tian SY, *et al.* Robust tri-color long persistent luminescence of phosphor-in-glass for outdoor application. *J Non Cryst Solids* 2020, **533**: 119830.
- [14] He QL, Hu CC. Optical properties of  $\text{SrAl}_2\text{O}_4:\text{Eu}^{2+}$  phosphor in glass. *Opt Mater* 2014, **38**: 286–289.
- [15] Yao CF, Jia ZX, Li ZR, *et al.* High-power mid-infrared

- supercontinuum laser source using fluorotellurite fiber. *Optica* 2018, **5**: 1264.
- [16] Denis G, Deniard P, Gautron E, *et al.* Structure and white luminescence of Eu-activated  $(\text{Ba,Sr})_{13-x}\text{Al}_{22-2x}\text{Si}_{10+2x}\text{O}_{66}$  materials. *Inorg Chem* 2008, **47**: 4226–4235.
- [17] Gebert W. Die kristallstruktur von  $\text{Ba}_{13}\text{Al}_{22}\text{Si}_{10}\text{O}_{66}$ . *Zeitschrift Für Kristallographie Cryst Mater* 1972, **135**: 437–452.
- [18] Terakado N, Sasaki R, Takahashi Y, *et al.* A novel method for stress evaluation in chemically strengthened glass based on micro-Raman spectroscopy. *Commun Phys* 2020, **3**: 37.
- [19] Galeener FL, Barrio RA, Martinez E, *et al.* Vibrational decoupling of rings in amorphous solids. *Phys Rev Lett* 1984, **53**: 2429–2432.
- [20] Sato T, Funamori N, Yagi T. Helium penetrates into silica glass and reduces its compressibility. *Nat Commun* 2011, **2**: 345.
- [21] Yadav AK, Singh P. A review of the structures of oxide glasses by Raman spectroscopy. *RSC Adv* 2015, **5**: 67583–67609.
- [22] Petrescu S, Constantinescu M, Anghel EM, *et al.* Structural and physico-chemical characterization of some soda lime zinc alumino-silicate glasses. *J Non Cryst Solids* 2012, **358**: 3280–3288.
- [23] Hu T, Ning L, Gao Y, *et al.* Glass crystallization making red phosphor for high-power warm white lighting. *Light Sci Appl* 2021, **10**: 56.
- [24] Cao WQ, Wang TW, Huang FF, *et al.* Tuning the micro-structure of germanosilicate glass to control  $\text{Bi}^0/\text{Bi}^+$  and promote efficient  $\text{Ho}^{3+}$  fluorescence. *Dalton Trans* 2018, **47**: 9717–9723.
- [25] Greskovich C, Prochazka S. Stability of  $\text{Si}_3\text{N}_4$  and liquid phase(s) during sintering. *J Am Ceram Soc* 1981, **64**: C-96–C-97.
- [26] Lin LT, Lv SC, Xie WQ, *et al.* Nanostructured glass composite for self-calibrated radiation dose rate detection. *Adv Opt Mater* 2021, **9**: 2100751.
- [27] Zhai BG, Huang YM. Green afterglow of undoped  $\text{SrAl}_2\text{O}_4$ . *Nanomaterials* 2021, **11**: 2331.
- [28] Lin XH, Zhang RL, Tian XM, *et al.* Coordination geometry-dependent multi-band emission and atypically deep-trap-dominated NIR persistent luminescence from chromium-doped aluminates. *Adv Opt Mater* 2018, **6**: 1701161.
- [29] Li YZ, Wang YH, Wang ZF, *et al.* White-light  $\text{Ba}_{13}\text{Al}_{22}\text{Si}_{10}\text{O}_{66}:\text{Eu}$  phosphor with bluish long afterglow via spontaneous reduction of  $\text{Eu}^{3+}$ . *J Electrochem Soc* 2010, **157**: J271.
- [30] Chen DQ, Xu M, Liu S, *et al.*  $\text{Eu}^{2+}/\text{Eu}^{3+}$  dual-emitting glass ceramic for self-calibrated optical thermometry. *Sens Actuat B Chem* 2017, **246**: 756–760.
- [31] Liu YS, Luo WQ, Zhu HM, *et al.* Optical spectroscopy of lanthanides doped in wide band-gap semiconductor nanocrystals. *J Lumin* 2011, **131**: 415–422.
- [32] Feng A, Michels S, Lamberti A, *et al.* Relating structural phase transitions to mechanoluminescence: The case of the  $\text{Ca}_{1-x}\text{Sr}_x\text{Al}_2\text{Si}_2\text{O}_8:1\%\text{Eu}^{2+},1\%\text{Pr}^{3+}$  anorthite. *Acta Mater* 2020, **183**: 493–503.
- [33] Qi Y, Zhang JS, Yu HQ, *et al.* Long persistent and photostimulated luminescence properties of  $\text{Sr}_2\text{Al}_2\text{SiO}_7:\text{Eu}^{2+}/\text{Tm}^{3+}$  phosphors. *J Rare Earth* 2016, **34**: 1–6.
- [34] Urbach, F. Zur lumineszenz der alkalihalogenide. *Sitzungsberichte Akad der Wiss Wien* 1930, **139**: 363–372.
- [35] Ueda J, Miyano S, Tanabe S. Formation of deep electron traps by  $\text{Yb}^{3+}$  codoping leads to super-long persistent luminescence in  $\text{Ce}^{3+}$ -doped yttrium aluminum gallium garnet phosphors. *ACS Appl Mater Interfaces* 2018, **10**: 20652–20660.
- [36] Pan ZW, Lu YY, Liu F. Sunlight-activated long-persistent luminescence in the near-infrared from  $\text{Cr}^{3+}$ -doped zinc gallogermanates. *Nat Mater* 2012, **11**: 58–63.
- [37] Liu JW, Liang YJ, Yan S, *et al.* Sunlight-activated long persistent luminescence in the ultraviolet-B spectral region from  $\text{Bi}^{3+}$ -doped garnet phosphors for covert optical tagging. *J Mater Chem C* 2021, **9**: 9692–9701.
- [38] Liu F, Chen YF, Liang YJ, *et al.* Phonon-assisted upconversion charging in  $\text{Zn}_3\text{Ga}_2\text{GeO}_8:\text{Cr}^{3+}$  near-infrared persistent phosphor. *Opt Lett* 2016, **41**: 954–957.
- [39] Chen XZ, Li Y, Huang K, *et al.* Trap energy upconversion-like near-infrared to near-infrared light rejuvenateable persistent luminescence. *Adv Mater* 2021, **33**: 2008722.
- [40] Nikl M, Yoshikawa A. Recent R&D trends in inorganic single-crystal scintillator materials for radiation detection. *Adv Opt Mater* 2015, **3**: 463–481.
- [41] Chen Q, Wu J, Ou X, *et al.* All-inorganic perovskite nanocrystal scintillators. *Nature* 2018, **561**: 88–93.
- [42] Ding DD, Li S, Xu H, *et al.* X-ray-activated simultaneous near-infrared and short-wave infrared persistent luminescence imaging for long-term tracking of drug delivery. *ACS Appl Mater Interfaces* 2021, **13**: 16166–16172.
- [43] Pei P, Chen Y, Sun CX, *et al.* X-ray-activated persistent luminescence nanomaterials for NIR-II imaging. *Nat Nanotechnol* 2021, **16**: 1011–1018.
- [44] Ou X, Qin X, Huang B, *et al.* High-resolution X-ray luminescence extension imaging. *Nature* 2021, **590**: 410–415.

**Open Access** This article is licensed under a Creative Commons Attribution 4.0 International License, which permits use, sharing, adaptation, distribution and reproduction in any medium or format, as long as you give appropriate credit to the original author(s) and the source, provide a link to the Creative Commons licence, and indicate if changes were made.

The images or other third party material in this article are included in the article's Creative Commons licence, unless indicated otherwise in a credit line to the material. If material is not included in the article's Creative Commons licence and your intended use is not permitted by statutory regulation or exceeds the permitted use, you will need to obtain permission directly from the copyright holder.

To view a copy of this licence, visit <http://creativecommons.org/licenses/by/4.0/>.